



Transforming rate capability through self-heating of energy-dense and next-generation batteries

Ryan S. Longchamps^a, Xiao-Guang Yang^a, Shanhai Ge^a, Teng Liu^a, Chao-Yang Wang^{a,b,*}

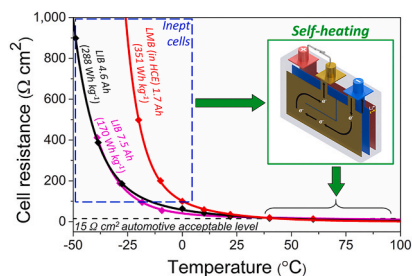
^a Electrochemical Engine Center (ECEC) and Department of Mechanical Engineering, The Pennsylvania State University, University Park, PA, 16802, USA

^b EC Power, 341 Science Park Road, State College, PA, 16803, USA

HIGHLIGHTS

- We present a highly energy-dense Li-ion battery that self-heats from $-50\text{ }^{\circ}\text{C}$.
- Significant power and energy are unlocked by rapid and uniform self-heating.
- Largest cell resistance suitable for self-heating is extended to $\sim 1000\text{ }\Omega\text{ cm}^2$.
- Potential for self-heating a lithium metal battery from $\geq -25\text{ }^{\circ}\text{C}$ is illustrated.

GRAPHICAL ABSTRACT



ARTICLE INFO

Keywords:

Lithium-ion battery
Low temperature
Energy density
Self-heating
Lithium metal battery

ABSTRACT

We demonstrate that an energy-dense, 288 Wh kg^{-1} lithium-ion battery can provide 152 Wh kg^{-1} energy and 1056 W kg^{-1} power at ultralow temperatures such as -40 or $-50\text{ }^{\circ}\text{C}$, contrary to virtually no performance expected under two simultaneous extremes: 4.04 mAh cm^{-2} cathode loading and $-40\text{ }^{\circ}\text{C}$. Unleashing this huge potential of current battery materials is achieved through a self-heating structure by embedding a micron-thin nickel foil in the electrochemical energy storage cell. The heating process from -40 to $10\text{ }^{\circ}\text{C}$ consumes only 5.1% of battery energy and takes 77 s. Further, based on the chemistry agnostic nature of self-heating, we present a generic chart to transform rate capability of lithium-ion and lithium metal batteries. These illustrative examples point to a new era of battery structure innovation, significantly broadening the performance envelopes of existing and emerging battery materials for electrified transportation.

1. Introduction

To enable universal access to the benefits of lithium-ion batteries (LIBs), they must be capable of operating in cold environments to, for example, warrant electric vehicle (EV) operation in the coldest of winters or support Martian surface exploration [1]. Unfortunately, low

temperatures pose a grand challenge for state-of-the-art (SOA) LIBs which suffer from substantial energy and power loss below $0\text{ }^{\circ}\text{C}$ down to a temperature of complete inoperability (ca. $-50\text{ }^{\circ}\text{C}$) [2]. Equally as critical, charging LIBs at practical rates below $0\text{ }^{\circ}\text{C}$ results in a rapid reduction of cycle life and attendant safety concerns primarily resulting from lithium plating on the graphite anode [3,4].

* Corresponding author. Electrochemical Engine Center (ECEC) and Department of Mechanical Engineering, The Pennsylvania State University, University Park, PA 16802, USA.

E-mail address: cwx31@psu.edu (C.-Y. Wang).

<https://doi.org/10.1016/j.jpowsour.2021.230416>

Received 30 May 2021; Received in revised form 10 July 2021; Accepted 21 August 2021

0378-7753/© 2021 Elsevier B.V. All rights reserved.

Common strategies to tackle the low-temperature issue focus on material modification, particularly on optimizing electrolytes, such as using solvents [5–10] of low melting points (e.g., esters) to reduce electrolyte viscosity and enhance ionic conductivity or developing new additives [6,11] and/or solvents [12] to enhance charge transfer kinetics at the electrode-electrolyte interfaces. While most of these studies report incremental improvements, rarely can they meet several important metrics simultaneously — achieving high discharge specific energy at practical C-rates with a long cycle life over a wide temperature range [13]. For instance, liquified electrolytes in cryogenic conditions yield remarkable performance and cyclability down to $-60\text{ }^{\circ}\text{C}$ [14,15], whereas the requisite pressure vessel for liquifying the electrolyte presents a significant barrier for battery production and use at room temperature (RT). Alternatively, moderate to high concentration electrolytes based on bis(trifluoromethylsulfonyl)amine and ethyl acetate have shown great retention of RT capacity at $-70\text{ }^{\circ}\text{C}$ when paired with either all organic or Li|polyimide electrodes [16,17]. Unfortunately, the former had a low specific energy (SE) of only 33 Wh kg^{-1} , and the latter retained 77% capacity after only 100 cycles. In general, such specialized batteries that can operate at temperatures below the LIB limits are in infancy and are hampered by low SE and/or short cycle life.

The demands for high SE pose a more considerable challenge to battery operation in cold environments. The U.S. Advanced Battery Consortium (USABC) is targeting 350 Wh kg^{-1} cell-level SE for EV batteries as compared to the 200–250 Wh kg^{-1} of SOA LIBs [18]. While new materials and chemistries (e.g., silicon or Li metal anode, solid-state electrolyte, etc.) show promising paths to even greater SE (500 Wh kg^{-1}), none of them, in the near term, can achieve a reasonable life at a practical C-rate even in RT. A prevailing approach to boost battery SE is to raise the areal loading of active materials (i.e., thicker electrode coatings) [19]. However, the well-known energy-power paradigm of an energy storage system begins to play a dominant role owing to the increased cell resistance with the presence of thick electrodes [20]. That is, maintaining high deliverable energy becomes an increasing challenge under high-power operation. In the case of two simultaneous extremes — ultra-cold temperatures and high areal loading design for high SE — the compounding effects render an apparent impasse for LIBs.

In contrast to the materials approach, heating lithium-ion cells to a workable temperature (e.g., $>0\text{ }^{\circ}\text{C}$) is a practical way to restore battery performance in cold environments. However, common external heating strategies face a conflict between heating speed and uniformity (that is, a high heating rate results in localized overheating near the cell surface), limiting the heating speed to $\sim 0.5\text{--}1\text{ }^{\circ}\text{C min}^{-1}$ [21,22]. In contrast, internal heating methods offer faster and more efficient cell heating [23]. In 2016, our group reported a new cell architecture, the self-heating battery (SHB), that embedded a thin nickel (Ni) foil as an internal cell heater [24], which achieved rapid and uniform heating of a medium-SE (170 Wh kg^{-1} , 2.0 mAh cm^{-2}), high-power Li-ion cell for plug-in hybrid EVs. However, for applications such as pure EVs, it is necessary to find out if self-heating can activate the most kinetically inhibiting materials and unleash both deliverable power and energy of the most energy-dense batteries of today (e.g., $>280\text{ Wh kg}^{-1}$) under extreme temperatures like -40 and $-50\text{ }^{\circ}\text{C}$. In this work, we present such a cell and provide experimental demonstrations of the remarkable power and energy of the SHB at temperatures down to $-50\text{ }^{\circ}\text{C}$, dramatically widening the performance window of current battery materials. Additionally, we combine direct-current resistance data of this LIB cell with a lithium metal battery (LMB) cell to construct a generic chart for transforming rate capability of current and emerging battery materials alike.

2. Materials and methods

2.1. Cell materials and fabrication

We fabricated 4.6 Ah SHB pouch cells using $\text{Li}(\text{Ni}_{0.8}\text{Co}_{0.1}\text{Mn}_{0.1})\text{O}_2$

(NMC811) as cathodes and graphite as anodes with 1 M LiPF_6 in ethylene carbonate/ethyl methyl carbonate (3:7 by weight) + 2% vinylene carbonate as electrolyte (Soulbrain, Michigan). The negative-to-positive capacity ratio was ~ 1.1 . The 4.6-Ah pouch cells used a stacked electrode design with 16 anode layers and 14 cathode layers. A ceramic-coated separator (Celgard 2325) of $25\text{ }\mu\text{m}$ thickness was used. A $25\text{-}\mu\text{m}$ -thick Ni foil sized at $112\text{ m}\Omega$ was coated with a thin layer of polyethylene terephthalate ($25\text{ }\mu\text{m}$, each side) for electrical insulation and sandwiched in the center of the cell stack adjacent to two single-sided anodes.

The cathodes were prepared by coating N-methylpyrrolidone-based slurry onto $13\text{ }\mu\text{m}$ Al foil, whose dry material consisted of 97.7 wt% NMC811. The anodes were prepared by coating deionized water-based slurry onto $8\text{ }\mu\text{m}$ Cu foil, whose dry weight consisted of 97.7 wt% graphite. The mass loadings of NMC811 and graphite were 20.8 and 13.1 mg cm^{-2} , respectively. Each SHB pouch cell had a $110\text{ mm} \times 80\text{ mm}$ footprint area, a thickness of 5.5 mm , weighed 72 g , and had a discharge capacity of 4.6 Ah at C/10 (4.3 Ah @ C/3). The ultrahigh areal loading of the electrodes in our experimental cells correspond to a specific energy of 288 Wh kg^{-1} and energy density of 682 Wh L^{-1} in a scaled-up 53 Ah format (Table S1).

We also developed a lithium metal pouch cell that was designed with parameters given in Table S1. For the electrolyte, battery-grade lithium bis(fluorosulfonyl)imide (LiFSI) salt, dimethoxyethane (DME) solvent, and triallyl phosphate (TAP) additive were sourced from Nippon Shokubai in Japan, Sigma-Aldrich, and TCI American, respectively. 1,1,2,2-Tetrafluoroethyl 2,2,3,3-tetrafluoropropyl ether (TTE) was used as an inert diluent (Synquest Laboratories, Inc.). The final composition of the electrolyte was LiFSI: DME: TTE = 1: 1.2 : 3 with 1 wt % TAP, and the LiFSI concentration in the electrolyte was $\sim 1.5\text{ M}$. The LMB is a 1.65 Ah pouch cell with energy density of 351 Wh kg^{-1} if scaled up to a 55 Ah size (Table S1).

2.2. Self-heating tests

All environmentally controlled tests were performed in an environmental chamber (Tenney Environmental), and charge and discharge tests were performed using a battery tester (Arbin BT-2000). All cell charging was performed at RT following the constant current-constant voltage (CC-CV) charging protocol with a charge rate of C/3, CC cut-off voltage of 4.2 V , CV cutoff current of C/20. For self-heating tests, a relay was wired between the ACT and positive terminals and controlled the heating process based on the cell surface temperature measured using a T-type thermocouple (Omega Engineering) adhered to the center of the cell surface. The Ni foil temperature was monitored during self-heating, rest, and discharge by measuring the resistance and utilizing the following empirical resistance temperature detector (RTD) calibration: $R_{\text{foil}} = 112\text{ m}\Omega[1 + 0.00456\text{ }^{\circ}\text{C}^{-1}(T - 21.6\text{ }^{\circ}\text{C})]$ with $R^2 = 0.999$. The self-heating current was measured via a shunt resistor placed in series with the relay. Prior to self-heating, the SHB was cooled in the environmental chamber by soaking for 4–8 h. For SHB heating performance characterization, self-heating was stopped when the cell surface temperature reached $5\text{ }^{\circ}\text{C}$. The self-heating rate was calculated as the difference between the maximum temperature after heating (after thermal equilibration) and the initial cell temperature divided by the time to reach $5\text{ }^{\circ}\text{C}$. The self-heating capacity consumption was calculated as the product of the average self-heating current and the self-heating time. The self-heating energy consumption was calculated as the product of the self-heating capacity and the open circuit voltage prior to self-heating, which remained approximately constant during self-heating due to low state-of-charge (SOC) change.

During self-heating, the fraction of heat generated by cell materials was determined by Eq. (1):

$$\frac{q_{\text{cell}}}{q_{\text{act}}} = \frac{\tau I (V_{\text{oc}} - V_{\text{cell}})}{\tau IV_{\text{oc}}} \quad (1)$$

where q_{cell} is the heat generated by cell materials, q_{act} is the total heat generation of the Ni foil and the cell materials, τ is the heating time, I is the self-heating current, V_{oc} is the open circuit voltage, and V_{cell} is the cell voltage (between the positive and negative terminals).

The fraction of heating energy lost from ohmic heat in the external switch/wiring during self-heating was calculated via Eq. (2):

$$\frac{q_{external}}{q_{act}} = \frac{\tau I (R_{external})}{\tau I V_{oc}} \quad (2)$$

where $q_{external}$ and $R_{external}$ are the ohmic heat loss and resistance of the external switch/wiring (i.e., between the positive and ACT cell terminals).

2.3. Peak power characterization

We performed 10-s hybrid pulse power characterization (HPPC) tests at a constant voltage of 2.7 V to characterize the peak discharge power. Prior to HPPC tests, all cells were fully charged, discharged to 80% SOC, and thermally equilibrated to the characterization temperature. For baseline cells, HPPC at 80% SOC was performed directly followed by a C/10 discharge to 50% SOC and a 1-h rest prior to the next HPPC pulse. For SHB cells, self-heating with a 5 °C cutoff temperature was performed followed by a 60-s relaxation period and the HPPC discharge pulse. The SHB was then discharged at C/10 to 50% SOC, cooled to the characterization temperature, and the HPPC test was repeated. The specific power (SP) was determined by multiplying the average HPPC discharge current times the constant voltage and then dividing by the cell mass.

To study the SHB peak power variation with heating time, the SHB HPPC test was repeated three times at 50% SOC in -40 °C ambient using time to terminate heating. Heating times of 65.8, 197.5, and 263.3 s were applied, corresponding to 0.5x, 1.5x, and 2x, respectively, relative to the 131.6 s heating time observed for the cell to reach 5 °C.

The effect of relaxation time on peak power was also explored by repeating the HPPC test at 80% SOC and in -10 °C ambient twice (Fig. S6). The 5 °C cutoff temperature remained unchanged, and the cell was relaxed for either 10 or 30 s after self-heating and prior to the HPPC pulse.

2.4. Deliverable energy characterization

All discharge energy characterization was performed beginning at 100% SOC by charging at RT as in the self-heating tests. The cells were then soaked in the environmental chamber for 4–8 h at the desired characterization temperature. For the baseline cells, CC discharge to a minimum cutoff voltage of 2.7 V was performed directly. For SHB cells, self-heating followed by relaxation was performed with the following test conditions. For 1C discharge, the cutoff temperature/relaxation time was 5 °C/10 s for ambients of -10, -20, -30, and -40 °C and 20 °C/210 s for -50 °C ambient. For 2C discharge, cutoff temperature/relaxation time of 5 °C/10 s were applied for -10 and -20 °C ambient while 10 °C/30 s, 15 °C/75 s, and 35 °C/330 s were applied for -30, -40, and -50 °C ambients, respectively. After relaxation, the cell was discharged to 2.7 V at either 1C or 2C. All C-rates were calculated relative to the C/3, RT cell capacity (e.g., 1C = 4.3A).

To account for SHB energy losses due to heat dissipation (temperature effect) and cell polarization from self-heating (polarization effect), three additional 1C discharge tests were performed in a -30 °C ambient. First, the baseline cell was discharged in 7.5 °C ambient ($SE_{baseline@7.5^\circ C}$), which represents the final equilibration temperature of the SHB after self-heating from -30 °C. For the SHB, the temperature effect was removed by performing self-heating as usual, after which supplemental, external electrical power was intermittently supplied to the Ni foil to maintain the cell temperature at 10 °C \pm 1 °C during discharge, which approximately represents the average cell temperature of the baseline case in 7.5 °C ambient. In this case, the discharge energy represented the

net SHB energy plus the energy lost due to the temperature effect ($SE_{SHB} + \Delta SE_{T \text{ effect}}$). The polarization effect was removed by heating the cell from -30 °C to 5 °C using only external power followed by a 10s relaxation period and standard discharge. In this case, only the temperature effect was present; thus, the discharge energy approximately represented the SHB energy plus the energy lost due to the polarization effect ($SE_{SHB} + \Delta SE_{pol \text{ effect}}$). Eq. (3) provides the approximation used for SHB energy accounting.

$$SE_{baseline@7.5^\circ C} \approx SE_{SHB} + \Delta SE_{ACT} + \Delta SE_{T \text{ effect}} + \Delta SE_{pol \text{ effect}} \quad (3)$$

2.5. Cycle life characterization

Cycle life testing of the baseline cell was performed at RT under the following conditions: C/3 CC-CV charge with C/10 cutoff current at 4.15 V, 5 min rest before discharge, 1C discharge to 2.7 V, and 5 min rest before charge. Reference performance capacity tests (Fig. S5d) were performed approximately every 100 cycles under the following conditions: C/3 CC-CV charge with 1-h CV step at 4.15 V, 30 min rest before discharge, and C/3 discharge to 2.7 V.

2.6. Direct current resistance characterization

Before measuring the direct current cell resistance (DCR), the cell SOC was set to 50% following the procedure in the HPPC tests. For temperatures at or above 0 °C, we performed a 10-s, CC discharge at 5C rate. For temperatures below 0 °C, the DCR was approximated from the first 10 s of self-heating. DCR is calculated with Eq. (4) where $A_{cath,tot}$ is the total cathode area for the respective cell, $V_{cell,10s}$ is the cell voltage at 10 s, and I_{avg} is the average current during the 10 s discharge.

$$DCR = A_{cath,tot} \frac{(V_{oc} - V_{cell,10s})}{I_{avg}} \quad (4)$$

2.7. Scaling to large-size 53 Ah cells

The experimental SHB specific discharge energy results were extrapolated to a scaled-up cell by multiplying the experimental results times the ratio of specific energies for the scaled-up cell and the experimental cell ($SE_{scaled-up}/SE_{experimental} = 288/234 = 1.231$). The specific power results from HPPC tests are presented for the scaled-up cell by multiplying the average experimental HPPC discharge C-rate times the C/3 capacity of the large-scale cell (50.8 Ah). This result was then multiplied by the constant HPPC voltage (2.7 V) and divided by the scaled-up cell mass (0.686 kg). The experimentally obtained heating rate was extrapolated to the scaled-up cell by multiplying times the specific energy ratio above (1.231) while the capacity/energy consumption per °C were extrapolated by dividing by the said ratio. These steps were taken in accordance with the proportionalities presented by Wang et al. [24]. It is important to note that the weight of the nickel foil was included in the weight of both the experimental and scaled-up cells; thus, the reported results take into account the effect of adding nickel foil on power and energy density. In general, the addition of nickel foil to a baseline cell only increases cell weight by ~1.5% [24].

3. Results and discussion

3.1. Self-heating from sub-zero temperatures

The SHB represents the first structural change to the cell design since the introduction of an electrochemical energy storage battery (Fig. 1a), involving the addition of a fourth component, a thin nickel foil, that holds the same footprint as the original three components (cathode, anode, and separator/electrolyte) [24]. Powered by the battery energy itself, the Ni foil plays the new role of regulating the battery temperature quickly and efficiently and hence modulating the battery state almost

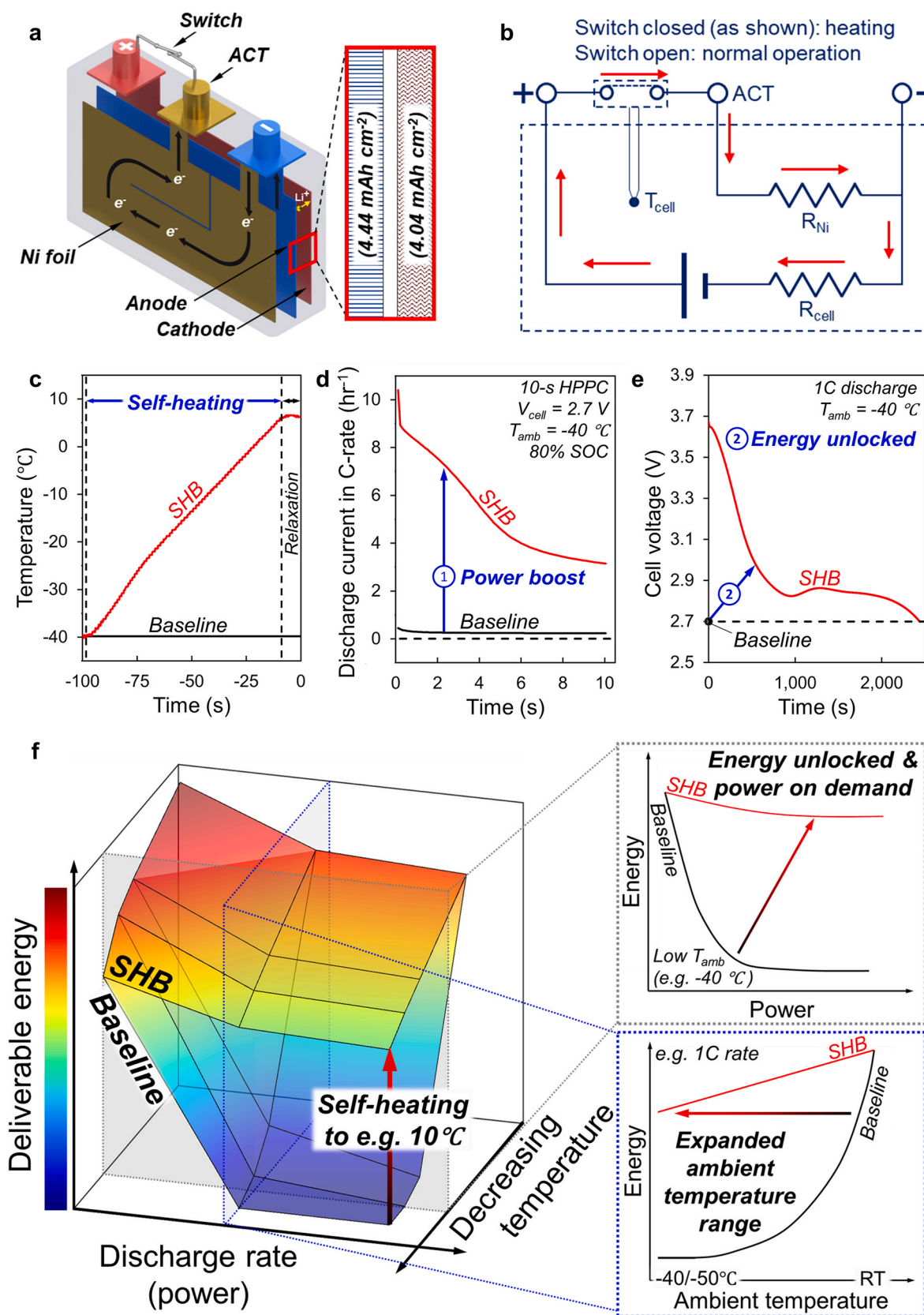


Fig. 1. Self-heating battery (SHB) vs. baseline Li-ion battery (LIB). (a) Self-heating structure with embedded nickel foil and energy-dense electrode loadings. (b) SHB electric circuit. (c)–(e) Comparison of SHB and baseline cells in -40°C ambient: (c) Cell temperature during self-heating; rapid heating enhances mass-transfer and electrochemical kinetics. (d) Hybrid pulse power characterization (HPPC) current evolution. (e) 1C discharge curves. The SHB yields dramatic power and deliverable energy improvement over the baseline. The C-rate in (d) and area under the discharge curves in (e) proportionally represent the power and delivered energy, respectively. (f) Deliverable energy vs. discharge rate and ambient temperature. The SHB overcomes the detrimental effects of low temperature and high power.

instantaneously. The Ni foil is sandwiched and electrically insulated between two single-sided anodes. One end of the Ni foil is welded with the anode tabs, and the other extends outside the cell to act as a third terminal, referred to herein as the “activation” (ACT) terminal. To initiate heating, an external switch between the positive and ACT terminals is closed, directing the discharge current through the nickel foil (Fig. 1b) to create immense internal heat that warms the cell rapidly (Fig. 1c). In turn, the SHB provides an immediate power boost (Fig. 1d) and a dramatic extension of the deliverable energy (Fig. 1e). Simply put, self-heating shifts the deleterious baseline energy-power-temperature trilemma to unleash the potential of the high-energy cell at ultra-low ambient temperatures and practical C-rates (Fig. 1f).

The linear dependence of Ni foil resistance on temperature also enables the foil as a resistance temperature detector, allowing measurement of the internal cell temperature. During self-heating, the maximum thru-plane temperature difference within the cell is measured as 14.7, 11.7, 6.7, 2.0, and <2.0 °C, from the ambient of -10 , -20 , -30 , -40 , and -50 °C, respectively. Note that this temperature nonuniformity vanishes in <15 s for all cases once heating is turned off (Fig. 2a, Figs. S1a, c, e, g). Better temperature uniformity with decreasing ambient temperature is attributed to an increased portion of heat generated by the cell materials as opposed to the Ni foil as well as a slower heating rate (Fig. 2c). For example, while self-heating from -10 and -40 °C, the average cell voltage shifts from 2.6 to 0.92 V with an average V_{oc} of ~ 4.15 V (Fig. 2b and Fig. S1b). Thus, heat generation from the cell materials represents 37 and 78% of the total, respectively, spatially evening out heat generation in the latter case. A multi-sheet

design can be adopted, where several parallel-connected Ni foils are distributed across the cell thickness direction to further reduce the thru-plane temperature difference while increasing the heating rate and reducing cell energy consumption [25,26].

Throughout the self-heating process from the -40 °C ambient, the battery discharge current and voltage remain steady at ~ 2 C rate and ~ 1 V (Fig. 2b). At higher ambient temperatures, such as -10 °C, the C-rate during self-heating is higher (ca. 5.5C; Figs. S1b, d, f, h) but still within the healthy operational range of electrodes, as supported by our previous study on the effects of self-heating on cycle life [24]. During heating, maintaining the cell voltage above 1 V is also vital to minimize potential capacity fade from copper dissolution due to over-discharge [27]. The short duration and low temperature of self-heating minimize the risk of copper dissolution and prevent any significant capacity fade from this mechanism [24]. In addition, optimal design of the nickel foil resistance can increase cell voltage during self-heating to achieve a balance between the concern of over-discharge and the heating rate.

In general, heating from various ambient conditions is stable as evidenced by the approximately linear trends in Fig. 2c and Fig. S2 (inset). Raising the cell temperature by ~ 47 °C (-40 to 6.6 °C) takes 87 s and consumes only 5.2% capacity and 5.9% energy in our experiment. At ambient temperatures above -30 °C, the experimental cell achieves a heating speed of ~ 1 °C s^{-1} . For -40 and -50 °C ambient, the heating rate decreases to 0.53 and 0.35 °C s^{-1} , respectively, which still far exceeds the speed of external heating methods (<0.02 °C s^{-1}).

The energy efficiency of self-heating is also remarkable due to the short duration which minimizes heat losses to the cold surroundings. In

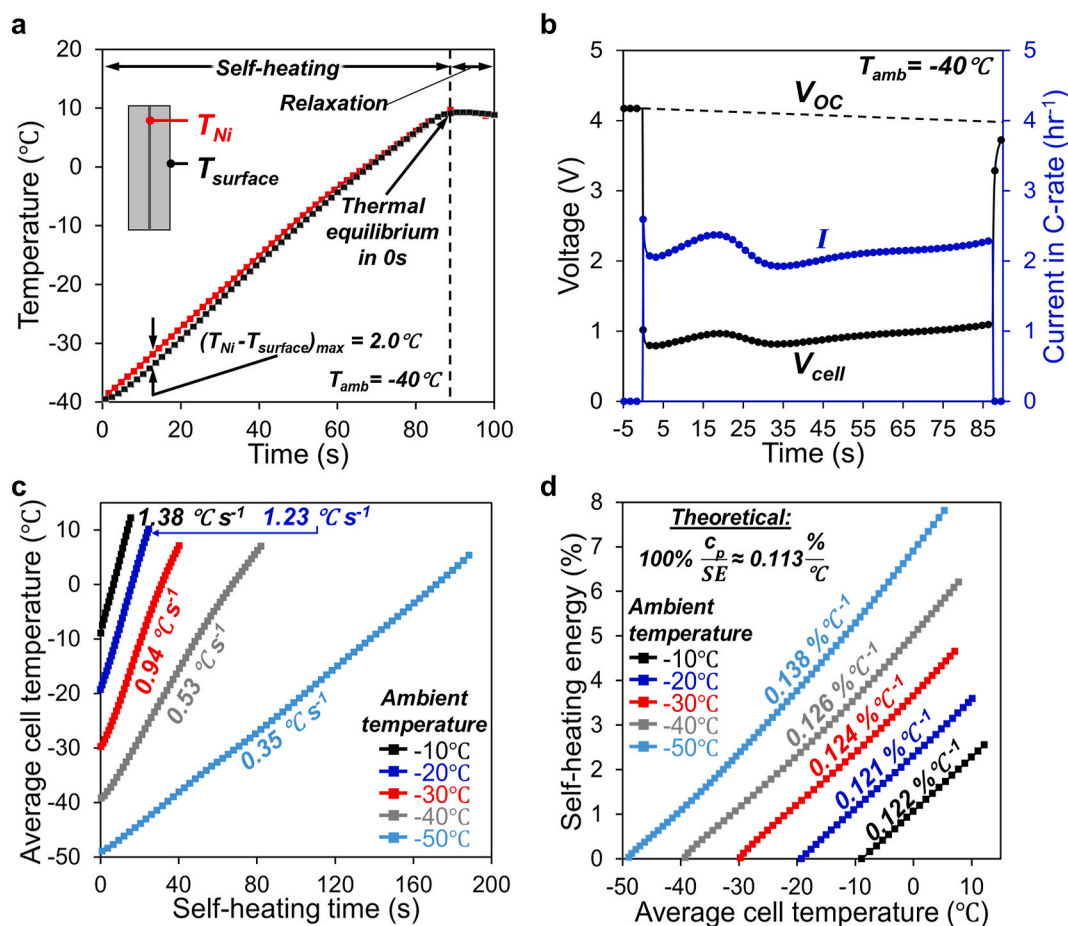


Fig. 2. Fast, uniform, and robust self-heating. (a) Nickel foil and surface temperatures during self-heating to ~ 10 °C from -40 °C ambient. (b) Corresponding cell voltage and self-heating current (C-rate) during self-heating. (c) Cell temperature evolutions upon heating. (d) Self-heating energy consumption vs. average cell temperature for heating. The theoretical estimate of energy consumption per °C is also given for the experimental cell, which has a specific heat of ~ 900 J kg^{-1} K^{-1} and a C/3 nominal specific energy of 221 Wh kg^{-1} .

Fig. 2d, the theoretical energy consumption per $^{\circ}\text{C}$ is calculated as $0.113\% \text{ }^{\circ}\text{C}^{-1}$, assuming a cell specific heat of $900 \text{ J kg}^{-1} \text{ K}^{-1}$. The experimental data closely matches the theoretical estimate, representing approximate heating efficiencies ranging from 82 to 93% for an ambient of -50 to $-10 \text{ }^{\circ}\text{C}$.

Of heating inefficiency, there is 3–5.2% lost as ohmic heat from the external switch and wiring for an ambient temperature range between -40 and $-10 \text{ }^{\circ}\text{C}$ based on an open circuit voltage before self-heating of $\sim 4.15 \text{ V}$ and an external wiring voltage drop (quantity IR_{external} in Eq. (2)) of 0.216 and 0.125 V , respectively. It is also important to note that the theoretical calculation is for the small experimental cell in this work. Scaling up to a 53 Ah , 288 Wh kg^{-1} cell using the same electrodes would further improve the heating efficiency due to higher energy density and hence a lower parasitic thermal mass fraction. In fact, all heating metrics are bolstered in a scaled-up cell; for example, the results for the large-size SHB at $-40 \text{ }^{\circ}\text{C}$ would improve to $0.091\% \text{ }^{\circ}\text{C}^{-1}$ for capacity consumption, $0.102\% \text{ }^{\circ}\text{C}^{-1}$ for energy consumption, and $0.65 \text{ }^{\circ}\text{C s}^{-1}$ for heating rate. Thus, raising the temperature of the 53 Ah SHB from -40 to $10 \text{ }^{\circ}\text{C}$ takes 77 s and consumes 5.1% energy.

The previous discussion pertains to self-heating from 100% state of charge (SOC). The SHB heating performance is also stable across a wide range of SOC. Repetitive self-heating and cooling cycles were performed in $-20 \text{ }^{\circ}\text{C}$ ambient after a single charge, spanning a range of 100 to $\sim 35\%$ SOC (Fig. S3a). The heating rate only decreases from $1.2 \text{ }^{\circ}\text{C s}^{-1}$ at 100% SOC to $0.85 \text{ }^{\circ}\text{C s}^{-1}$ at 35% SOC, requiring only 31.6 s for heating in the latter case (Fig. S3b). Even at such a low SOC, the capacity and energy consumptions are only 3.4 and 3.3% of the nominal values,

respectively (Figs. S3c and d). At the extreme low temperature of $-50 \text{ }^{\circ}\text{C}$ and low SOC of 40%, the SHB can still self-heat at $0.098 \text{ }^{\circ}\text{C s}^{-1}$ with energy consumption of $0.183\% \text{ }^{\circ}\text{C}^{-1}$ (Fig. S4). Albeit slower, the heating rate near the lowest temperature of battery operability is still between 6x and 12x faster than external heating methods.

3.2. Low-temperature power and energy

The peak power of the baseline and SHB cells in relevant ambient conditions and at various SOC is plotted in Fig. 3a relative to that at room temperature. The baseline cell specific power (SP) is impractically low at 4.0 and 1.6% of the RT power at -40 and $-50 \text{ }^{\circ}\text{C}$ (80% SOC), while the SHB retains $\sim 47\%$ under the same conditions (Fig. 3a). After extrapolating to practical values for the 53 Ah cell, the baseline cell delivers 2221 W kg^{-1} peak SP (see Fig. S5c for experimental baseline SP) at RT and 80% SOC; thus, the SHB can still provide 1056 and 1051 W kg^{-1} in -40 and $-50 \text{ }^{\circ}\text{C}$ ambient, respectively, as compared to 89 and 36 W kg^{-1} of the baseline cell, boosting the battery power by 12x and 29x, respectively, in -40 and $-50 \text{ }^{\circ}\text{C}$ ambient and 80% SOC (Fig. 3c). Remarkably, SHB power at these extreme low temperatures is still much higher than the USABC target of 700 W kg^{-1} for electric vehicle batteries in a $30 \text{ }^{\circ}\text{C}$ environment [18]! Note that the higher power boost shown in Fig. 3c for 50% SOC as compared to 80% SOC in the $-50 \text{ }^{\circ}\text{C}$ ambient may be attributed to decreasing measurement accuracy as baseline power becomes extremely low. The SHB power boost decreases at lower SOC, but in $-40 \text{ }^{\circ}\text{C}$ and at 50% SOC, the SHB still provides 38% of RT power compared to the 3.4% of the baseline, representing a 12x increase

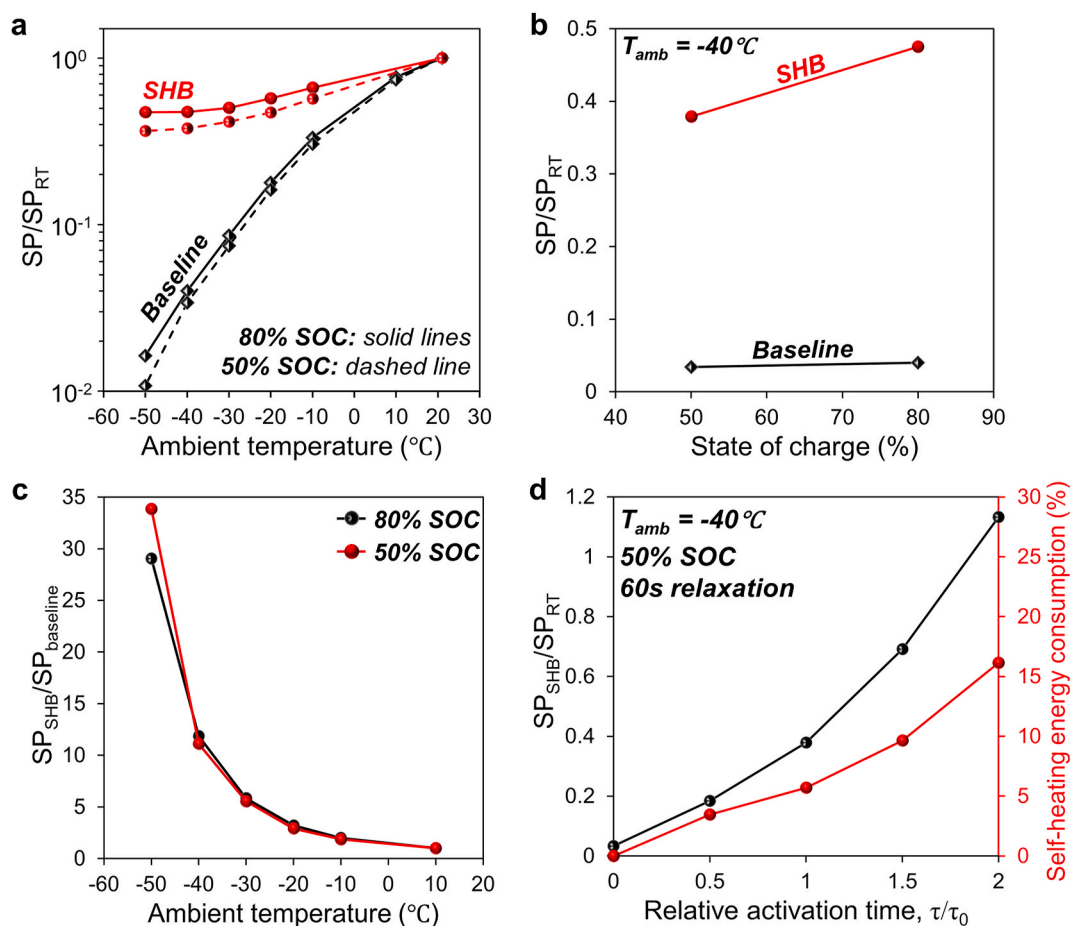


Fig. 3. SHB power boost over baseline. (a) 10-s HPPC specific discharge power (SP) of the SHB and baseline cells relative to the SP at room temperature (RT) at 80% and 50% state of charge (SOC). (b) SP relative to RT-SP vs. SOC for the baseline and SHB cells in $-40 \text{ }^{\circ}\text{C}$ ambient. (c) SHB-to-baseline SP ratio vs. ambient temperature for 50 and 80% SOC. (d) 50% SOC HPPC power normalized to that at RT and percentage energy consumption vs. the self-heating time relative to that for heating to $6.6 \text{ }^{\circ}\text{C}$ with a cutoff temperature of $5 \text{ }^{\circ}\text{C}$ (τ_0).

to 706 W kg^{-1} (Fig. 3b and c). Additionally, the SHB power can be further increased by extending the heating time to increase the cell operating temperature (Fig. 3d). When the heating time is doubled in the -40°C ambient (i.e., the cell is heated to 67°C), the SHB power soars to 2112 W kg^{-1} at 50% SOC, exceeding that of the baseline cell at RT (1793 W kg^{-1}).

During HPPC experiments, a 60-s rest period was applied between self-heating and the discharge pulse to relax the concentration gradients generated by the high-current discharge during self-heating. In application, adding tens of seconds to the relaxation time can have a dramatic effect on power, which increased from 69 to 86% of baseline power at 10°C when the relaxation was extended from 10 to 60 s in -10°C (Fig. S6). With a 60-s relaxation, for example, a car owner only needs to wait ~ 100 s to drive with sufficient power in -30°C , a minimal sacrifice compared to tens of minutes of heating (waiting) time for conventional, externally-heated EV battery powertrains.

Not only does the SHB provide a rapid boost in discharge power, a step change in discharge energy is also obtained. The baseline cell shows the expected significant loss of energy at low temperatures in Fig. 4a, delivering effectively zero energy at -30°C and 1C rate ($>99.8\%$ loss). At 2C (Fig. 4b), the cell energy already drops to zero at -20°C ($>99.6\%$ loss). In contrast, the SHB maintains 61% (147 Wh kg^{-1}) of the RT energy at 1C and 65% (152 Wh kg^{-1}) at 2C in -40°C ambient. Moreover,

the SHB can overcome the significant challenge of -50°C ambient, unleashing 51% (123 Wh kg^{-1}) and 59% (137 Wh kg^{-1}) of RT energy at 1C and 2C, respectively. The further improvement of discharge energy at 2C is ascribed to larger heat generation during discharge which helps maintain the cell temperature after self-heating (Figs. S2 and S7).

The SHB is not expected to recover 100% of RT energy. First, the cell in our test is heated to ca. 10°C , not RT. In fact, the SHB does not achieve a final temperature of 10°C after heating in all ambient environments, owing to varying thermal inertia when heating stops (Figs. 2c and S2 (inset)). In -30°C ambient, the cell only reaches $\sim 7.5^\circ\text{C}$. To determine the maximum energy the SHB could deliver for such an experimental protocol, we measured the discharge energy during a baseline discharge test with 7.5°C ambient (Fig. S8a). When normalized to this result, the SHB in -30°C delivered 83.9% of the baseline energy while the heating energy represents 6.5%, corresponding to a total of 90.4% (Fig. S8d). During SHB discharge, the cell temperature initially decreases during the establishment of a quasi-steady-state condition in the surrounding insulation materials, followed by a temperature rise largely from increased heat generation at low SOC (Figs. S2 and S7). The net result is a lower average discharge temperature (5.5°C in -30°C ambient) and an associated loss of discharge energy, herein referred to as the temperature effect. Additionally, the strong cell polarization from self-heating induces an accelerated decrease in voltage at the early stages

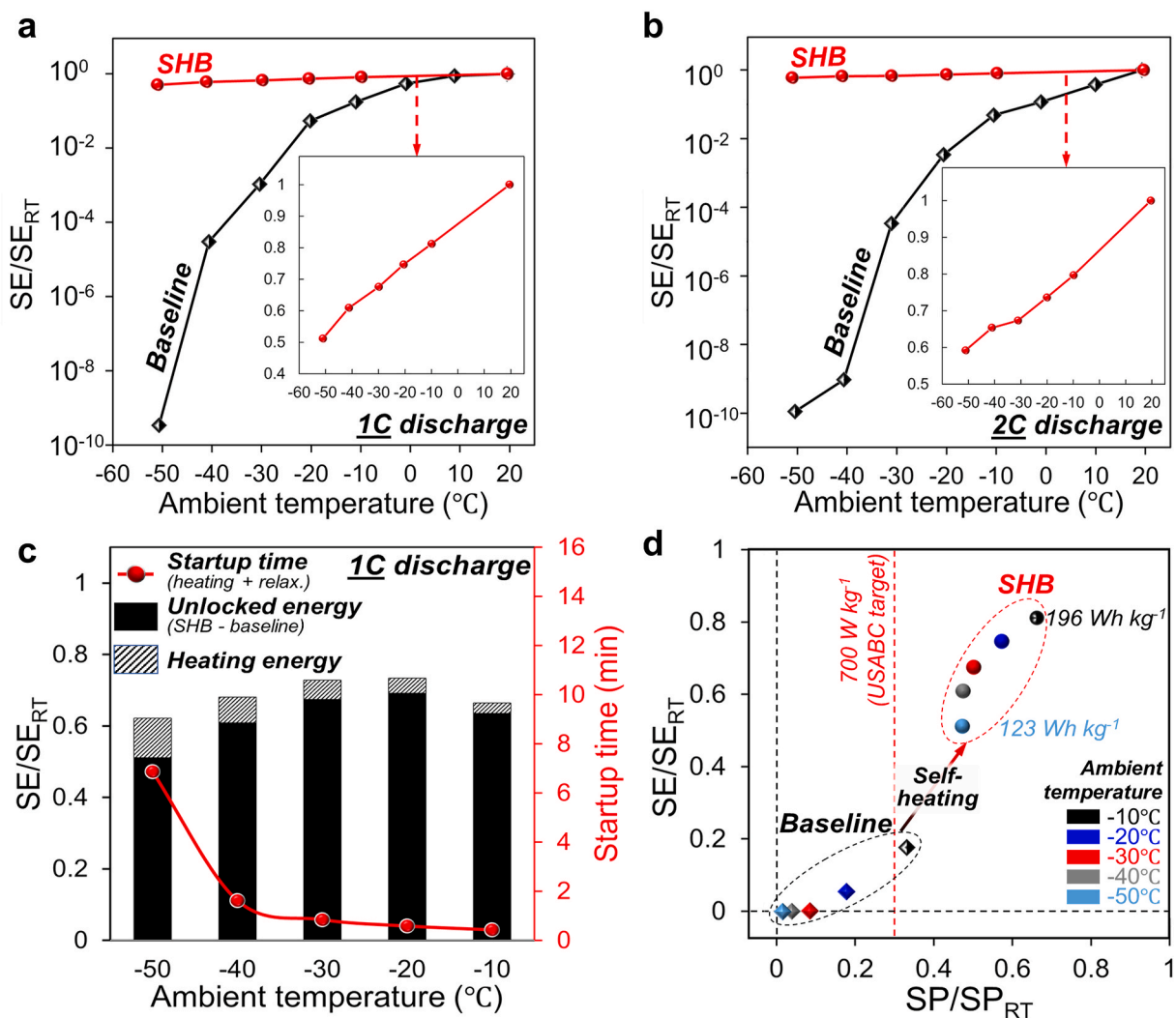


Fig. 4. Deliverable energy at low ambient temperatures. (a) 1C and (b) 2C discharge specific energy relative to that at RT (linear scale for SHB in inset) vs. ambient temperature for the SHB and baseline cells. (c) Energy unlocked, heating energy, and startup time at 1C rate vs. ambient temperature. (d) Relative to RT: 1C discharge energy vs. 80% SOC HPPC specific power for ambient temperatures of -10 , -20 , -30 , -40 , and -50°C .

of discharge, also reducing the discharge energy. We term this the polarization effect. When each effect is isolated, the temperature and polarization effects represent 4.5 and 3.5% of the energy losses, respectively (Figs. S8c and d), which account for a majority of the remaining 9.6% energy under question. A better thermal boundary condition and slower heating (e.g., through intermittent self-heating or larger Ni foil resistance) offer remedies to reduce both temperature and polarization effects, respectively.

Fig. 4c summarizes the sacrifice to achieve the benefit of unlocked energy for 1C discharge. In the ultralow ambient temperatures of -40 and -50 °C, extended heating and relaxation times are applied to overcome the increased heat dissipation and greater cell polarization, resulting in an increased startup time of 1.6 and 6.9 min, respectively, as compared to >1 hr. for external heating. When averaged across all ambient temperatures, the SHB unlocks 62% of the RT energy (150 Wh kg^{-1}) at a cost of 6.1% cell energy used for heating and 2.1 min startup time. Thus, as an assessment of return on investment, the unlocked energy of the SHB is ~ 10 x the energy utilized for heating.

Simultaneously augmenting the limited baseline power and energy performance is required for realizing the potential of a given battery chemistry in an ultracold ambient. Fig. 4d plots the 1C discharge energy vs. the peak power at 80% SOC, both normalized to that at RT for the respective cells. The baseline cell data lie in the lower left corner near the origin, implying that the cell is largely dormant and unable to release its stored energy. Despite the significant challenges of the extreme cold and energy-dense cell design, self-heating effectively activates the battery materials and restores sufficient power and useable energy, lifting the SHB grouping toward RT performance. This represents a large expansion of the performance window of the batteries of today through a simple structure innovation that maintains the robust cycle life of the optimized chemistry (Fig. S5d).

Fig. 4d also raises a big question whether one should continue to pursue new material discovery to improve low-temperature performance at the expense of sacrificing high-temperature stability and safety, a usual trade-off for all materials. A new opportunity now exists

for future development of battery materials to focus solely on maximizing high-temperature stability and safety while leaving the provision of low-temperature performance to self-heating structures.

3.3. Transforming rate capability of current and emerging battery materials

The ability to self-heat with battery energy is chemistry agnostic, depending only on the battery internal resistance. Fig. 5 compares the temperature-dependence of direct-current resistance (DCR) for the 288 Wh kg^{-1} LIB in this work with that of the 170 Wh kg^{-1} LIB reported earlier, where the upper limit of DCR for successful self-heating was constrained to $\sim 400 \text{ } \Omega \text{ cm}^2$ [24]. It is now possible for a cell possessing an initial DCR as high as $1000 \text{ } \Omega \text{ cm}^2$ to thermally modulate to room temperature, achieving a DCR as low as $15 \text{ } \Omega \text{ cm}^2$, which is suitable for electric vehicles. Expansion of the DCR upper limit from 400 to $1000 \text{ } \Omega \text{ cm}^2$ for successful self-heating, enabled by combination of the highly energy-dense LIB cell and ultracold temperatures in the present work, is significant as the DCR level of $1000 \text{ } \Omega \text{ cm}^2$ is indicative of extremely inept batteries. For instance, applying 1C current (i.e. 4 mA cm^{-2}) to the present cell would immediately incur ohmic voltage drop of 4 V, dropping cell voltage to virtually zero. Thus, the ability of self-heating initially is rather weak. However, a little heating will dramatically lower the DCR, as can be seen from Fig. 5, and hence increase the battery discharge rate for much more heating. Such a strong positive-feedback effect provides a scientific mechanism for the present self-heating structure to “wake up” dormant batteries and substantially transform their rate capability.

Finally, it is of interest to extend Fig. 5 to a vast majority of advanced battery materials such as lithium metal batteries (LMBs), all-solid-state batteries, Mg and Na batteries, all of which are presently hampered by impractically low current densities and kinetically inhibited materials [28–31], i.e. exhibiting very high DCRs. To provide a specific example, we developed the LMB detailed in section 2.2 and Table S1. The measured DCR of the LMB cell is also plotted in Fig. 5 as a function of

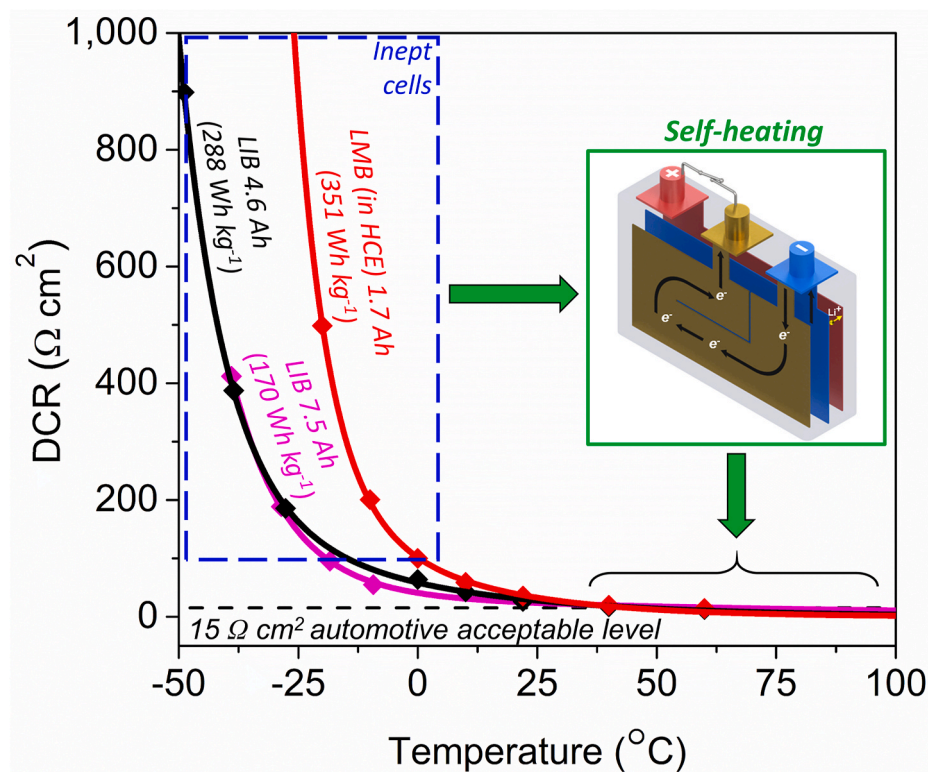


Fig. 5. Chemistry-agnostic transformation of rate capability through self-heating. The internal resistance of the 288 Wh kg^{-1} graphite||NMC811 cells in this work can be transformed to acceptable levels for automotive applications when self-heating is harnessed. This result expands the upper limit of DCR for successful self-heating to 1000 from $400 \text{ } \Omega \text{ cm}^2$ previously established for a 170 Wh kg^{-1} LIB [24]. Such an advance implies that self-heating of 351 Wh kg^{-1} lithium metal||NMC811 cells can enable high-rate operation at temperatures as low as ca. -25 °C.

temperature. It is seen that the LMB DCR is much higher than the 288 Wh kg⁻¹ LIB and already reaches ~1000 Ω cm² around -25 °C (vs. -50 °C in the LIB) primarily due to higher viscosity of the high concentration electrolyte. The automotive acceptable level, i.e. 15 Ω cm², can only be met at cell temperatures between 40 and 60 °C. Nonetheless, it follows from Fig. 5 that one can still modulate this highly energy-dense LMB cell in any ambient temperature down to -25 °C to the 40–60 °C range, thereby transforming its rate capability to levels acceptable for automotive applications.

4. Conclusions

Here, we have shown that the self-heating structure can overcome ultracold environments down to -50 °C even when energy-dense, rate-limiting designs are employed (288 Wh kg⁻¹ with 4.04 mAh cm⁻²). Delivery of practical levels of energy (≥137 Wh kg⁻¹ at 2C rate) and power (≥1051 W kg⁻¹) in extremely harsh conditions is demonstrated with currently available LIB materials via rapid (e.g., tens of seconds), efficient (~90%), and uniform (i.e., <15s for thermal equilibration) self-heating. The present study also extends the upper limit of cell resistance for successful self-heating to ~1000 Ω cm², which begins to cover the range of a vast majority of next-generation, highly energy-dense battery technologies, such as the LMB presented in this work (351 Wh kg⁻¹). Thus, the self-heating structure reported herein offers synergy between material and structure innovation to aid the successful and expeditious development of the batteries of tomorrow. Future work consists of building more next-generation batteries, such as all solid-state batteries, and adding their DCR data in Fig. 5.

CRediT authorship contribution statement

Ryan S. Longchamps: Methodology, Formal analysis, Investigation, Data curation, Writing – original draft, Writing – review & editing, Visualization. **Xiao-Guang Yang:** Methodology, Writing – original draft. **Shanhai Ge:** Resources, Investigation. **Teng Liu:** Investigation. **Chao-Yang Wang:** Conceptualization, Writing – review & editing, Supervision, Project administration, Funding acquisition.

Declaration of competing interest

The authors declare that they have no known competing financial interests or personal relationships that could have appeared to influence the work reported in this paper.

Acknowledgments

Financial support from Pennsylvania Department of Environmental Protection (DEP) (DEP grant # 4100068680-1) and the William E. Diefenderfer Endowment is gratefully acknowledged.

Appendix A. Supplementary data

Supplementary data to this article can be found online at <https://doi.org/10.1016/j.jpowsour.2021.230416>.

References

- M.C. Smart, B.V. Ratnakumar, R.C. Ewell, S. Surampudi, F.J. Puglia, R. Gitzendanner, The use of lithium-ion batteries for JPL's Mars missions, *Electrochim. Acta* 268 (2018) 27–40, <https://doi.org/10.1016/j.electacta.2018.02.020>.
- G. Zhu, K. Wen, W. Lv, X. Zhou, Y. Liang, F. Yang, Z. Chen, M. Zou, J. Li, Y. Zhang, W. He, Materials insights into low-temperature performances of lithium-ion batteries, *J. Power Sources* 300 (2015) 29–40, <https://doi.org/10.1016/j.jpowsour.2015.09.056>.
- M. Petzl, M. Kasper, M.A. Danzer, Lithium plating in a commercial lithium-ion battery – a low-temperature aging study, *J. Power Sources* 275 (2015) 799–807, <https://doi.org/10.1016/j.jpowsour.2014.11.065>.
- X.-G. Yang, G. Zhang, S. Ge, C.-Y. Wang, Fast charging of lithium-ion batteries at all temperatures, *Proc. Natl. Acad. Sci. Unit. States Am.* 115 (2018) 7266–7271, <https://doi.org/10.1073/pnas.1807115115>.
- L.F. Xiao, Y.L. Cao, X.P. Ai, H.X. Yang, Optimization of EC-based multi-solvent electrolytes for low temperature applications of lithium-ion batteries, *Electrochim. Acta* 49 (2004) 4857–4863, <https://doi.org/10.1016/j.electacta.2004.05.038>.
- M.C. Smart, B.V. Ratnakumar, S. Surampudi, Y. Wang, X. Zhang, S.G. Greenbaum, A. Hightower, C.C. Ahn, B. Fultz, Irreversible capacities of graphite in low-temperature electrolytes for lithium-ion batteries, *J. Electrochem. Soc.* 146 (1999) 3963, <https://doi.org/10.1149/1.1392577>.
- M.C. Smart, B.V. Ratnakumar, S. Surampudi, Electrolytes for low-temperature lithium batteries based on ternary mixtures of aliphatic carbonates, *J. Electrochem. Soc.* 146 (1999) 486, <https://doi.org/10.1149/1.1391633>.
- E.J. Plichta, W.K. Behl, A low-temperature electrolyte for lithium and lithium-ion batteries, *J. Power Sources* 88 (2000) 192–196, [https://doi.org/10.1016/S03787753\(00\)00367-0](https://doi.org/10.1016/S03787753(00)00367-0).
- S.S. Zhang, K. Xu, J.L. Allen, T.R. Jow, Effect of propylene carbonate on the low temperature performance of Li-ion cells, *J. Power Sources* 110 (2002) 216–221, [https://doi.org/10.1016/S0378-7753\(02\)00272-0](https://doi.org/10.1016/S0378-7753(02)00272-0).
- M.C. Smart, B.V. Ratnakumar, K.B. Chin, L.D. Whitcanack, Lithium-ion electrolytes containing ester cosolvents for improved low temperature performance, *J. Electrochem. Soc.* 157 (2010) A1361, <https://doi.org/10.1149/1.3501236>.
- Q. Li, S. Jiao, L. Luo, M.S. Ding, J. Zheng, S.S. Cartmell, C.-M. Wang, K. Xu, J.-G. Zhang, W. Xu, Wide-temperature electrolytes for lithium-ion batteries, *ACS Appl. Mater. Interfaces* 9 (2017) 18826–18835, <https://doi.org/10.1021/acsami.7b04099>.
- J. Xu, X. Wang, N. Yuan, B. Hu, J. Ding, S. Ge, Graphite-based lithium ion battery with ultrafast charging and discharging and excellent low temperature performance, *J. Power Sources* 430 (2019) 74–79, <https://doi.org/10.1016/j.jpowsour.2019.05.024>.
- M.C. Smart, B.V. Ratnakumar, S. Surampudi, Use of organic esters as cosolvents in electrolytes for lithium-ion batteries with improved low temperature performance, *J. Electrochem. Soc.* 149 (2002) A361, <https://doi.org/10.1149/1.1453407>.
- Y. Yang, Y. Yin, D.M. Davies, M. Mayer, Y. Zhang, E.S. Sablina, S. Wang, J.Z. Lee, O. Borodin, C.S. Rustomji, Y.S. Meng, Liquefied gas electrolytes for wide-temperature lithium metal batteries, *Energy Environ. Sci.* 13 (2020) 2209–2219, <https://doi.org/10.1039/D0EE01446J>.
- C.S. Rustomji, Y. Yang, T.K. Kim, J. Mac, Y.J. Kim, E. Caldwell, H. Chung, Y. S. Meng, Liquefied gas electrolytes for electrochemical energy storage devices, *Science* 356 (2017), eaal4263, <https://doi.org/10.1126/science.aal4263>.
- X. Dong, Zhaowei Guo, Ziyang Guo, Y. Wang, Y. Xia, Organic batteries operated at -70 °C, *Joule* 2 (2018) 902–913, <https://doi.org/10.1016/j.joule.2018.01.017>.
- X. Dong, Y. Lin, P. Li, Y. Ma, J. Huang, D. Bin, Y. Wang, Y. Qi, Y. Xia, High-energy rechargeable metallic lithium battery at -70 °C enabled by a cosolvent electrolyte, *Angew. Chem.* 131 (2019) 5679–5683, <https://doi.org/10.1002/ange.201900266>.
- J.P. Christophersen, Battery Test Manual for Electric Vehicles, Revision 3, 2015, <https://doi.org/10.2172/1186745>. United States: N.
- K.G. Gallagher, S.E. Trask, C. Bauer, T. Woehrl, S.F. Lux, M. Tschech, P. Lamp, B. J. Polzin, S. Ha, B. Long, Q. Wu, W. Lu, D.W. Dees, A.N. Jansen, Optimizing areal capacities through understanding the limitations of lithium-ion electrodes, *J. Electrochem. Soc.* 163 (2015) A138, <https://doi.org/10.1149/2.0321602jes>.
- H. Zheng, J. Li, X. Song, G. Liu, V.S. Battaglia, A comprehensive understanding of electrode thickness effects on the electrochemical performances of Li-ion battery cathodes, *Electrochim. Acta* 71 (2012) 258–265, <https://doi.org/10.1016/j.electacta.2012.03.161>.
- Y. Ji, C.Y. Wang, Heating strategies for Li-ion batteries operated from subzero temperatures, *Electrochim. Acta* 107 (2013) 664–674, <https://doi.org/10.1016/j.electacta.2013.03.147>.
- X.-G. Yang, T. Liu, C.-Y. Wang, Innovative heating of large-size automotive Li-ion cells, *J. Power Sources* 342 (2017) 598–604, <https://doi.org/10.1016/j.jpowsour.2016.12.102>.
- A. Mistry, A. Verma, P.P. Mukherjee, Controllable electrode stochasticity self-heats lithium-ion batteries at low temperatures, *ACS Appl. Mater. Interfaces* 11 (2019) 26764–26769, <https://doi.org/10.1021/acsami.9b05468>.
- C.-Y. Wang, G. Zhang, S. Ge, T. Xu, Y. Ji, X.-G. Yang, Y. Leng, Lithium-ion battery structure that self-heats at low temperatures, *Nature* 529 (2016) 515–518E, <https://doi.org/10.1038/nature16502>.
- G. Zhang, S. Ge, T. Xu, X.-G. Yang, H. Tian, C.-Y. Wang, Rapid self-heating and internal temperature sensing of lithium-ion batteries at low temperatures, *Electrochim. Acta* 218 (2016) 149–155, <https://doi.org/10.1016/j.electacta.2016.09.117>.
- X.-G. Yang, G. Zhang, C.-Y. Wang, Computational design and refinement of self-heating lithium ion batteries, *J. Power Sources* 328 (2016) 203–211, <https://doi.org/10.1016/j.jpowsour.2016.08.028>.
- H. Maleki, J.N. Howard, Effects of overdischarge on performance and thermal stability of a Li-ion cell, *J. Power Sources* 160 (2006) 1395–1402, <https://doi.org/10.1016/j.jpowsour.2006.03.043>.
- M. Pasta, D. Armstrong, Z.L. Brown, J. Bu, M.R. Castell, P. Chen, A. Cocks, S. A. Corr, E.J. Cussen, E. Darnbrough, V. Deshpande, C. Doerrer, M.S. Dyer, H. El-Shinawi, N. Fleck, P. Grant, G.L. Gregory, C. Grovener, L.J. Hardwick, J.T.S. Irvine, H.J. Lee, G. Li, E. Liberti, I. McClelland, C. Monroe, P.D. Nellist, P.R. Shearing, E. Shoko, W. Song, D.S. Jolly, C.I. Thomas, S.J. Turrell, M. Vestli, C.K. Williams, Y. Zhou, P.G. Bruce, On solid-state batteries, roadmap, *J. Phys. Energy* 2 (2020), 032008, <https://doi.org/10.1088/2515-7655/ab95f4>, 2020.

- [29] P. Albertus, S. Babinec, S. Litzelman, A. Newman, Status and challenges in enabling the lithium metal electrode for high-energy and low-cost rechargeable batteries, *Nature Energy* 3 (2018) 16–21, <https://doi.org/10.1038/s41560-017-0047-2>.
- [30] N.J. Taylor, S. Stangeland-Molo, C.G. Haslam, A. Sharafi, T. Thompson, M. Wang, R. Garcia-Mendez, J. Sakamoto, Demonstration of high current densities and extended cycling in the garnet Li₇La₃Zr₂O₁₂ solid electrolyte, *J. Power Sources* 396 (2018) 314–318, <https://doi.org/10.1016/j.jpowsour.2018.06.055>.
- [31] P. Canepa, G. Sai Gautam, D.C. Hannah, R. Malik, M. Liu, K.G. Gallagher, K. A. Persson, G. Ceder, Odyssey of multivalent cathode materials: open questions and future challenges, *Chem. Rev.* 117 (2017) 4287–4341, <https://doi.org/10.1021/acs.chemrev.6b00614>.